



Numerical experiment based on non-linear micropolar finite element to study micro-rotations generated by the non-symmetric Maxwell stress tensor

Roberto Palma¹ · José L. Pérez-Aparicio² · Robert L. Taylor³

Received: 21 November 2022 / Accepted: 25 April 2023
© The Author(s) 2023

Abstract

The main aim of the present work is to investigate the role of the Maxwell stress tensor in the study of active materials. Despite the importance of this tensor in modeling mechatronic devices used in sophisticated applications, its non-symmetry still generates controversies in the literature, probably because classical continuum mechanics assumes a symmetric Cauchy stress, although the sum of Cauchy and Maxwell stresses is non-symmetric. In the framework of generalised continuum mechanics—a more advanced formalism than the classical one—, each material point has an associated microstructure so that the micro-rotations of the electric/magnetic dipoles present in real active materials may be simulated. To this end, a modified total stress formulation, including an angular momentum balance, is developed and implemented into a finite element research code using a complex-step formulation. It is concluded that generalised mechanics allows for incorporating both symmetric and non-symmetric contributions of the Maxwell tensor. Consequently, the rotations generated by the electromagnetic field may be analysed. The influence of the complete Maxwell tensor in a magnetostrictive actuator is studied by several magneto-mechanical numerical experiments of a Terfenol-D rod encircled by air, and several conclusions are highlighted.

Keywords Finite Element Method · Maxwell stress tensor · Non-symmetry · Generalised Continuum Mechanics · Micro-rotations · Magnetostrictive materials

1 Introduction

Active materials, such as piezoelectrics and piezomagnetics, are used in mechatronic devices due to their inherent ability to combine mechanical and electromagnetic fields by two separate couplings: the first can be modelled by constitutive equations—obtained from thermodynamic potentials—, and the second by electromagnetic body forces, commonly incorporated into the linear momentum balance by the Maxwell Stress Tensor (MST).

Physically, the origin of these couplings comes from two separate interactions, see [27, 31]:

- Short-range forces (local effects) due to interatomic interactions among material points inside the body that generate both forces and couples.
- Long-range forces (non-local effects) that emerge from the interactions between material points and external fields.

The short-range forces, see [37, 39], are closely related with the piezoelectric/piezomagnetic constitutive equations, some reported in [15]. As mentioned, the contribution of these forces to the linear momentum balance is often obtained from thermodynamic potentials, see [10, 13].

The long-range forces are commonly expressed as the divergence of the MST for an amenable implementation in numerical approaches such as the Finite Element (FE) method. However, the MST is non-symmetric in transversely isotropic materials such as piezoelectrics and piezomagnetics [25, 34, 37]. This lack of symmetry has generated a compre-

✉ Roberto Palma
rpalgue@ugr.es

¹ Department of Structural Mechanics and Hydraulic Engineering, University of Granada, Granada, Spain

² Department of Continuum Mechanics and Theory of Structures, Universitat Politècnica de València, Valencia, Spain

³ Department of Civil and Environmental Engineering, University of California at Berkeley, California, USA

hensive discussion in the literature since Noether's theorem [21] states that the angular momentum must be conserved, and non-symmetric stress tensors do not automatically fulfil this condition. For this reason, [31] reported that the non-symmetric MST does not have physical meaning since it is caused by the transformation of the electromagnetic long-range body forces into the short-range divergence of the MST.

Despite the importance of the MST in modelling mechatronic devices (for instance, for vibrations and noise control), it should be considered in many research works, for example, in [29, 32]. This is due to two main difficulties:

- ▷ the non-linearity
- ▷ the possible non-symmetry

The first difficulty is nowadays easily overcome by non-linear algorithms and sophisticated computer codes. But the second remains unsolved since the proper solution is not clear from a theoretical point of view, even if it is essential since the MST skew-symmetric part can generate electromagnetic torques as argued in [6, 14].

On this ground, two main approaches based on Classical Continuum Mechanics (CCM) may be found in the literature to model active materials considering the MST:

- (i) Analytically, [1, 2, 19, 37] introduce a symmetric total stress tensor as the sum of two non-symmetric tensors: a Cauchy-like stress tensor and the MST itself. FE models using this total stress are reported in [11, 22, 28, 30, 38].
- (ii) The numerical approach from [25] allows us to calculate electromagnetic torques and forces with a nodal force method. The torques are expanded into non-local (long-range) and local (short-range) terms, the latter due to the MST non-symmetric part.

Although the controversy on the MST non-symmetry was partially clarified through physical arguments in [19, 37], the main novelty of the present work is to establish the CCM limitations (including the use of the MST itself) to model active materials. For this purpose, a Generalised Continuum Mechanics (GCM) approach based on the Micropolar Mechanics (MM) theory is developed; see [17] for a general description of MM. Roughly, this theory extends CCM assuming that each material point in the continuum is associated with a micro-rigid body and, consequently, three micro-rotations are incorporated to the FE degrees of freedom (dofs).

Based on MM, in the current work both linear and angular momentum balances are stated, concluding that the MST holds a skew-symmetric part. Furthermore, the electromagnetic torque generated by this non-symmetry may only be studied with MM since, in the framework of CCM, each

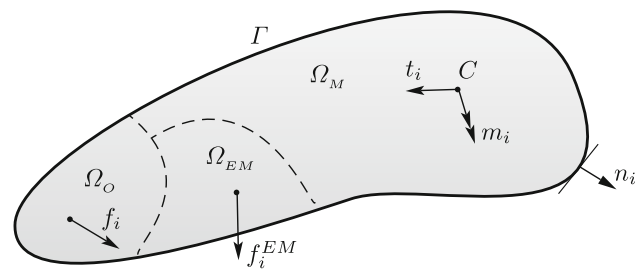


Fig. 1 Domain $\Omega = \Omega_{EM} \cup \Omega_M \cup \Omega_O$ with boundary Γ and outward normal n_i . The domain is under electromagnetic f_i^{EM} , mechanical traction t_i , couple stress vector m_i , and other body forces f_i

material point lays in the position of its centre of mass [24]. Then the point only transmits linear momentum to neighbours, not micro-rotations. As demonstrated in [19, 37], the absence of rotation implies that the MST must be symmetric for basic CCM.

Finally, and for completeness, a numerical study based on the FE method is developed to obtain some conclusions on the influence of the MST using MM. In particular, a mini-magnetostrictive actuator made out of the transversely isotropic Terfenol-D material is simulated. Four numerical experiments are developed, demonstrating that the micro-rotations can be of the macro order for magnetic fields of normal levels. Also, regardless of intensity, not all magnetic fields can produce rotations.

Dynamic effects are not considered in the present work for simplicity, and for the FE formulation, only the magneto-mechanical coupling is considered.

For clarity, index notation is used throughout the present work. Non-symmetric tensors are denoted by $(\cdot)_{ij}$, with their symmetric and skew-symmetric parts denoted by $(\cdot)_{(ij)}$ and $(\cdot)_{[ij]}$, respectively. In addition, the alternating third-order and identity second-order tensors are denoted by e_{ijk} and δ_{ij} . Finally, the Einstein summation convention is used throughout the document.

2 Balance equations

Consider a domain $\Omega = \Omega_{EM} \cup \Omega_M \cup \Omega_O$ and its boundary Γ , containing electromagnetic Ω_{EM} , mechanical Ω_M and other Ω_O matter, as shown in Fig. 1. The present section states the balances of linear and angular momentum considering electromagnetic forces $f_i^{EM} \in \Omega_{EM}$, mechanical forces represented by traction t_i and couple stress m_i vectors so that $\{t_i, m_i\} \in \Omega_M$. Other body forces $f_i \in \Omega_O$ are included for completeness due to long-range effects such as gravitation.

As introduced before, MM considers that each material point has an associated microstructure mathematically represented by a trihedron at each material point C . Consequently, the microstructure is modelled as a rigid body

adding three micro-rotations θ_i to the three classical macro-displacements u_i .

For the most general case, the electromagnetic forces f_i^{EM} are composed of:

- Long-range forces from electromagnetic source: free electric charge density ρ_q^f and free electric current j_i^f .
- Short-range forces due to polarisation P_i and magnetisation M_i vectors related to the material media.

The vectors t_i and m_i exclusively represent short-range forces. The former is the classical traction related to a generic stress tensor σ_{ij} by the Cauchy relation of (1) top. The latter is due to the microstructure, and it is related to the couple stress tensor τ_{ij} of (1) bottom, also by a Cauchy-like relation:

$$\begin{aligned} t_i &= \sigma_{ji} n_j, \\ m_i &= \tau_{ji} n_j. \end{aligned} \tag{1}$$

Notice that both σ_{ij} and τ_{ij} are *a priori* non-symmetric tensors.

2.1 Electromagnetic forces

Continuum Electrodynamics is founded on a set of four empirical laws called Maxwell equations [28] expressed as:

$$\begin{aligned} D_{i,i} &= \rho_q^f, \\ B_{i,i} &= 0, \\ (E_j e_{ijk})_{,i} + \frac{\partial B_k}{\partial t} &= 0, \\ (H_j e_{ijk})_{,i} - \frac{\partial D_k}{\partial t} - j_k^f &= 0, \end{aligned} \tag{2}$$

where E_i , D_i , H_i , and B_i denote electric field, electric displacement, magnetic field, and magnetic induction, respectively. In addition, t denotes time and ∂ partial derivative. The electromagnetic constitutive equations that relate P_i and M_i vectors are defined as:

$$\begin{aligned} D_i &= P_i + \epsilon_0 E_i, \\ B_i &= \mu_0 (H_i + M_i), \end{aligned} \tag{3}$$

where ϵ_0 and μ_0 are the vacuum permittivity and permeability, respectively.

The balance of linear electromagnetic momentum is obtained from Poynting's theorem [28] and in quasi-static regime is expressed as:

$$f_i^{EM} = \sigma_{ji}^{EM}, \tag{4}$$

where σ_{ji}^{EM} is the mathematical symbol for the MST. There exist at least four expressions [9] for f_i^{EM} or σ_{ji}^{EM} , but the present work uses:

$$\sigma_{ji}^{EM} = D_j E_i + B_j H_i - \left(\frac{D_k D_k}{\epsilon_0} + \frac{B_k B_k}{\mu_0} \right) \frac{\delta_{ji}}{2}, \tag{5}$$

According to [39] the previous expression satisfies the electromagnetic boundary conditions and may be obtained from a thermodynamic formulation as in [10] or from energy-momentum considerations as in [8].

Since any tensor may uniquely be decomposed into symmetric and skew-symmetric parts, the MST is split into both by introducing (3) into (5) to give:

$$\begin{aligned} \sigma_{(ij)}^{EM} &= \frac{P_j E_i + P_i E_j}{2} + \frac{\mu_0}{2} (M_j H_i + M_i H_j) + \\ &\epsilon_0 E_i E_j + \mu_0 H_i H_j - \left(\frac{D_k D_k}{\epsilon_0} + \frac{B_k B_k}{\mu_0} \right) \frac{\delta_{ij}}{2}, \\ \sigma_{[ji]}^{EM} &= \frac{P_j E_i - P_i E_j}{2} + \frac{\mu_0}{2} (M_j H_i - M_i H_j), \end{aligned} \tag{6}$$

where the second contribution represents the tensor form of the classical electromagnetic torque.

According to [23], applying the divergence theorem to the total MST allows to transform the long-range forces f_i^{EM} into short-range ones by:

$$t_i^{EM} = \sigma_{ji}^{EM} n_j, \tag{7}$$

where t_i^{EM} denotes the Maxwell traction vector.

2.2 Total linear momentum balance

From Noether's theorem, the linear momentum must be conserved since the Lagrangian (function of movement) must be independent of the origin. Considering both mechanical and electromagnetic forces, the balance of linear momentum establishes the relationship between long-range and short-range forces by:

$$\int_{\Gamma} (t_i + t_i^{EM}) d\Gamma + \int_{\Omega} f_i d\Omega = 0, \tag{8}$$

Applying the divergence theorem to the previous first integral, taking into account (1) top and (7), the local form of (8) becomes:

$$(\sigma_{ji} + \sigma_{ji}^{EM})_{,j} + f_i = 0. \tag{9}$$

2.3 Total angular momentum balance

Also, from Noether's theorem, the angular momentum must be explicitly conserved since the Lagrangian function must be independent of the measurement angle. Depending on the material constitution, the MST skew-symmetric part may be:

- ▷ $\sigma_{[ij]}^{EM} = 0$, then the angular momentum balance is automatic stated.
- ▷ $\sigma_{[ij]}^{EM} \neq 0$, then the angular momentum balance must be explicitly guaranteed in the formulation.

With x_i denoting the position vector that locates each material point, for the second case and applying the definition of angular momentum, the second balance reads:

$$\int_{\Gamma} \left[e_{ijk} x_i (t_j + t_j^{EM}) + m_k \right] d\Gamma + \int_{\Omega} e_{ijk} x_i f_j d\Omega = 0. \quad (10)$$

Again, the divergence theorem may be applied to the first term on the left-hand side of (10). Taking into account (1) bottom and (9), the balance of angular momentum in local form reads:

$$\tau_{ji,j} + e_{ijk} (\sigma_{jk} + \sigma_{jk}^{EM}) = 0. \quad (11)$$

3 On the symmetry of the Maxwell tensor

Based on the equations of the previous section, the main objectives are now: i) to analyse the CCM limitations to study the MST skew-symmetric part, ii) to formulate a new approach based on MM to include the MST skew-symmetric part. To address i), a revision of the different approaches for the MST is conducted.

3.1 Classical continuum mechanics approaches

In the CCM framework, the couple stress tensor and the micro-rotations are absent: $\tau_{ji} = \theta_i = 0$. In this context, at least three approaches exist to study the MST in the literature. The most important approaches are listed to highlight the absence of rotations.

3.1.1 Rinaldi

This approach was developed in [31] and is grounded on the lack of physical meaning in the mixture of long- and short-range forces. Specifically, even though the long-range force f_i^{EM} (called *maxwellian* in the reference) may be mathematically expressed as a short-range force t_i^{EM} related with

σ_{ji}^{EM} , as in (7), the reference argues that (7) is not unique but "arbitrary to within an additive divergence-less tensor". In this context, [20] also discusses the wrong "conceptual replacement" since t_i^{EM} has no physical sense "unless it is integrated over a closed surface".

Rinaldi concludes that the short-range forces must exclusively come from the classical and symmetric Cauchy stress tensor $\sigma_{(ij)}^C$. Consequently, the linear (9) and angular (11) balances simplify to:

$$\begin{cases} \sigma_{(ij),j}^C + f_i^{EM} + f_i = 0, \\ e_{ijk} \sigma_{(jk)}^C = 0 \Rightarrow \sigma_{(ij)}^C = \sigma_{(ji)}^C, \end{cases} \quad (12)$$

Finally, Rinaldi remarks that f_i^{EM} can only be replaced by σ_{ji}^{EM} if the electromagnetic torque is added to (12) bottom.

3.1.2 Eringen

This approach reported in [4] modifies the balance of linear electromagnetic momentum (4) by splitting f_i^{EM} as the sum of long-range Lorentz f_i^L and of short-range ponderomotive f_i^{PM} forces:

$$f_i^{EM} = f_i^L + f_i^{PM} = \sigma_{(ij),j}^{EM} + \sigma_{[ji],j}^{EM}. \quad (13)$$

Also, Eringen argues that f_i^{PM} only generates angular momentum, and therefore, it is not included in the linear momentum (9):

$$(\sigma_{(ji)}^C + \sigma_{(ji)}^{EM}),_j + f_i = 0. \quad (14)$$

3.1.3 Total stress

This approach is the most published: [1, 2, 19, 37]. It is grounded in the definition of a symmetric total stress $\sigma_{(ij)}^T$ as the sum of a non-symmetric and Cauchy-like tensor σ_{ij} plus the MST tensor:

$$\sigma_{(ij)}^T = \underbrace{\sigma_{(ij)}^C - \sigma_{[ij]}^{EM}}_{\sigma_{ij}} + \underbrace{\sigma_{(ij)}^{EM} + \sigma_{[ij]}^{EM}}_{\sigma_{ij}^{EM}} = \sigma_{(ij)}^C + \sigma_{(ij)}^{EM}. \quad (15)$$

As argued in [1], this $\sigma_{(ij)}^T$ includes both long-range (electromagnetic) and short-range (mechanical) forces and satisfies boundary conditions. Along that line, the reference criticised Rinaldi's approach for not considering proper boundary conditions. Still within CCM, the linear (9) and angular (11) balances become:

$$\begin{cases} \sigma_{(ij),j}^T + f_i = (\sigma_{(ij)}^C + \sigma_{(ij)}^{EM}),_j + f_i = 0, \\ e_{ijk} \sigma_{(jk)}^T = 0 \Rightarrow \sigma_{[ij]}^C = -\sigma_{[ij]}^{EM}, \end{cases} \quad (16)$$

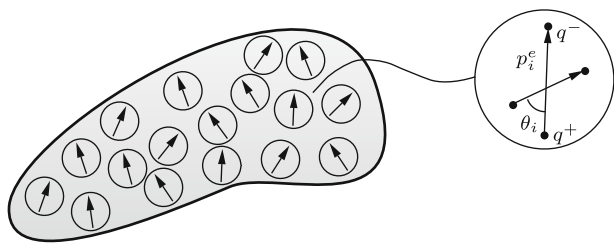


Fig. 2 Polarisable body composed of electric dipoles p_i^e defined by two electric charges q^+, q^- represented by rigid bodies (zoom): stretching and rotation of p_i^e under electric field

This approach results in the same set of equations as (13) of Eringen from the previous subsection.

3.2 Micropolar mechanics

As commented, CCM represents each material point only by its centre of mass. A more sophisticated formalism such as MM can better describe the electric and magnetic dipole rotations at the micro-continuum scale.

Consider the polarisable medium shown in Fig. 2 (the same arguments hold for magnetisable media) composed of electric dipoles q_i , defined by two electric charges q^+, q^- . As observed in the zoom and argued in [7], q_i will stretch and rotate an angle θ_i upon application of an electric field. CCM captures the stretch, but a GCM approach such as MM must be used to study the rotation. Under this approach, the balances of linear and angular momentum read:

$$\begin{cases} (\sigma_{(ij)}^C + \sigma_{[ji]}^C + \sigma_{ji}^{EM}),_j + f_i = 0, \\ \tau_{ji,j} + e_{ijk}(\sigma_{[jk]}^C + \sigma_{[jk]}^{EM}) = 0, \end{cases} \quad (17)$$

where $\sigma_{[ji]}^C$ may be considered null in a first approximation, see Sect. 4. Notice that with this nullity and according to [18], $\sigma_{[jk]}^{EM}$ is closely related to a parameter called coupling number, which depends on the microstructure (intrinsic lattice size scale) of each material.

In conclusion, the current MM approach has several advantages, allowing to:

- sum the symmetric Cauchy $\sigma_{(ij)}^C$ to the non-symmetric Maxwell σ_{ji}^{EM} , since the angular momentum balance is fulfilled by the additional (17) bottom.
- use the classical constitutive equations of piezoelectrics and/or piezomagnetism (see Sect. 4) since they are expressed using only the symmetric part $\sigma_{(ij)}^C$.
- calculate the rotation of the electric/magnetic dipoles, and from it, the generated electromagnetic torque τ_{ji} , relevant for mechatronic devices.

- recover the standard total stress method if the microstructure is not considered and $\tau_{ji} = 0$.

4 Magnetostrictive governing equations

This section particularises the MM governing equations for the magnetostrictive problem used in the numerical experiments of Sect. 6. Seven dofs are considered: three macro-displacements u_i , three micro-rotations θ_i , and the scalar magnetic potential φ .

The governing equations comprise balance (linear and angular) momenta, compatibility equations, boundary conditions, and material constitution. For the sake of clarity, this section summarises all equations.

4.1 Balance equations

The balance equations for the MM approach given in (17) are rewritten here without the separation into symmetric and skew-symmetric contributions. In addition, the magnetic field is balanced by the Gauss law, the second of (2) to obtain:

$$\begin{aligned} \sigma_{ji,j} + f_i &= 0, \\ \tau_{ji,j} - 2\sigma_i^\times &= 0, \\ B_{i,i} &= 0 \end{aligned} \quad (18)$$

Assuming $\sigma_{[ji]}^C = 0$, the tensor σ_{ji} without the electric field and the new pseudo-vector σ_i^\times read:

$$\begin{aligned} \sigma_{ji} &= \sigma_{(ij)}^C + B_j H_i - \frac{B_k B_k}{2\mu_0} \delta_{ji}, \\ \sigma_i^\times &= -\frac{1}{2} e_{ijk} \sigma_{jk}, \end{aligned} \quad (19)$$

where the latter may be expressed in matrix form as:

$$\{\sigma_i^\times\} = \frac{1}{2} \begin{Bmatrix} B_3 H_2 - B_2 H_3 \\ B_1 H_3 - B_3 H_1 \\ B_2 H_1 - B_1 H_2 \end{Bmatrix}. \quad (20)$$

4.2 Compatibility equations

Again, two compatibility equations must be considered due to the existence of mechanical and magnetic fields. For the former, the strain measures—energetically conjugated to σ_{ji} and τ_{ji} from the first and second (18)—may be obtained from the additive decomposition of motion shown in Fig. 3. Then, the total deformation process may be mathematically represented by the gradient of macro-displacements $u_{j,i}$ composed of:

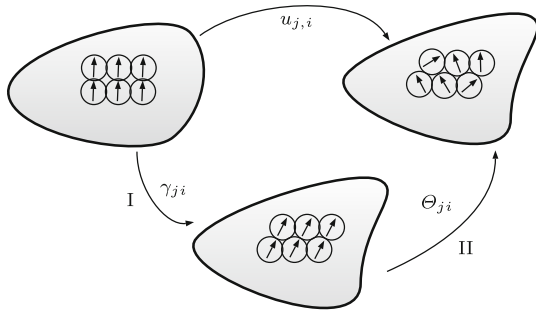


Fig. 3 Micropolar mechanics deformation process, combining mechanical deformations and dipole micro-rotations, as in Fig. 2

- I A mechanical deformation given by γ_{ji} .
 II A pure rotation of the microstructure given by the skew-symmetric tensor $\Theta_{ji} = -e_{jik}\theta_k$.

Unlike the CCM model, for which there is only one strain measure, in the MM framework and as in some beam theories, there are two deformation measures:

$$\gamma_{ji} = u_{j,i} - e_{ijk}\theta_k, \quad \chi_{ji} = \theta_{j,i}, \quad (21)$$

where χ_{ji} is the gradient of micro-rotations. As observed, the CCM strain measure is recovered without micro-rotations.

The magnetic compatibility equation may be obtained by applying Helmholtz's theorem to the last Maxwell law (2) without electric terms to get:

$$(H_j e_{ijk})_{,i} = 0 \Rightarrow H_i = -\varphi_{,i} \quad (22)$$

4.3 Material constitution

The piezomagnetic constitutive equations used in the numerical experiments of Sect. 6 are presented as a set of four equations:

$$\begin{aligned} \sigma_{(ij)}^C &= C_{ijkl}u_{k,l} - e_{ijk}^{\varphi}H_k, & \sigma_{[ij]}^C &= -\bar{C}_{ijkl}e_{klm}\theta_m, \\ B_i &= e_{ijk}^{\varphi}u_{j,k} + \mu_{ij}H_j, & \tau_{ij} &= C_{ijkl}^*\chi_{kl}, \end{aligned} \quad (23)$$

where C_{ijkl} , e_{ijk}^{φ} , μ_{ij} and C_{ijkl}^* are the elastic fourth-order tensor, piezomagnetic third-order tensor, magnetic permeability second-order tensor and micro-elastic fourth-order tensor, respectively. Furthermore, a new fourth-order tensor denoted by \bar{C}_{ijkl} depends on the coupling number, see [18], assumed to be zero in the present work for simplicity.

Assuming the nine-component Voigt notation of Table 1 and considering that the material is magnetised along the x_3

Table 1 Tensorial notation with double indices $(\cdot)_{ij}$ and equivalent Voigt notation with single indices $(\cdot)_I$

| Tensorial | 11 | 22 | 33 | 12 | 21 | 23 | 32 | 31 | 13 |
|-----------|----|----|----|----|----|----|----|----|----|
| Voigt | 1 | 2 | 3 | 4 | 5 | 6 | 7 | 8 | 9 |

direction as shown in Fig. 5, these constitutive tensors may be expressed in matrix forms as in the Appendix 1. For C_{ijkl}^* , the two micromechanical material coefficients l_t and l_b are the twisting and bending characteristic lengths; see [17].

4.4 Boundary conditions

For this coupled formulation, Dirichlet (essential) Γ_D and Neumann (natural) Γ_N boundary conditions are split into mechanical (Γ_D^u, Γ_N^u) and magnetic ($\Gamma_D^{\varphi}, \Gamma_N^{\varphi}$), satisfying:

$$\begin{aligned} \Gamma_D^u \cup \Gamma_N^u &= \Gamma; & \Gamma_D^u \cap \Gamma_N^u &= \emptyset; \\ \Gamma_D^{\varphi} \cup \Gamma_N^{\varphi} &= \Gamma; & \Gamma_D^{\varphi} \cap \Gamma_N^{\varphi} &= \emptyset; \end{aligned}$$

Denoting by \bar{u}_i and $\bar{\varphi}$ the prescribed displacements and scalar magnetic potential; and by \bar{t}^C the prescribed Cauchy traction, both boundary conditions may be expressed as:

$$\begin{aligned} \text{Dirichlet :} & \quad u_i = \bar{u}_i, & \varphi &= \bar{\varphi}. \\ \text{Neumann :} & \quad t_i n_i = \bar{t}^C, & B_i n_i &= 0. \end{aligned} \quad (24)$$

Notice that there are no natural boundary conditions for the MST since they emerge from the body forces; see (4).

5 Finite element formulation

This section briefly describes the Finite Element (FE) formulation conducted to implement the theoretical MM formulation reported in Sect. 4. In particular, a three-dimensional, non-linear, and displacement-based FE equation set is developed. There are no geometrical non-linearities since small strain is considered, but the MST introduces material non-linearities that quadratically depend on the magnetic field, as shown in (20) top. For this reason, the FE formulation has two peculiarities:

- ▷ It is based on three residuals: linear and angular momentum balances plus magnetic Gauss law, to be explicitly defined in (28).
- ▷ A complex-step formulation with a perturbation parameter h_n is conducted, as explained in [12, 16, 35].

5.1 Weak forms

To obtain the weak forms, the balance equations (18) are multiplied by test functions $\delta u_i, \delta \theta_i, \delta \varphi$ of the dofs and integrated over the whole domain Ω :

$$\begin{aligned} \int_{\Omega} \delta u_i (\sigma_{ji,j} + f_i) \, d\Omega &= 0, \\ \int_{\Omega} \delta \theta_i (\tau_{ji,j} - 2\sigma_i^\times) \, d\Omega &= 0, \\ \int_{\Omega} \delta \varphi B_{i,i} \, d\Omega &= 0. \end{aligned} \tag{25}$$

Applying the divergence theorem to the first term on the left-hand side of each (25), the final weak forms become:

$$\begin{aligned} - \int_{\Omega} \delta u_{i,j} \sigma_{ji} \, d\Omega + \int_{\Gamma} \delta u_i t_i \, d\Gamma + \int_{\Omega} \delta u_i f_i \, d\Omega &= 0, \\ - \int_{\Omega} \delta \theta_{i,j} \tau_{ji} \, d\Omega + \int_{\Gamma} \delta \theta_i m_i \, d\Gamma - \int_{\Omega} \delta \theta_i 2\sigma_i^\times \, d\Omega &= 0, \\ - \int_{\Omega} \delta \varphi_{,i} B_i \, d\Omega &= 0. \end{aligned} \tag{26}$$

5.2 Discretisations and residuals

In the present FE formulation, eight-noded elements with standard Lagrange functions N^a at node a are used for the discretisation. In particular, the dofs and their test functions may be expressed by an isoparametric formulation as:

$$\begin{aligned} u_i &\approx N_i^a \mathcal{I}(\bar{u}_i^a), \quad \theta_i \approx N_i^a \mathcal{I}(\bar{\theta}_i^a), \quad \varphi \approx N_i^a \mathcal{I}(\bar{\varphi}_i^a), \\ \delta u_i &\approx N_i^a \mathcal{I}(\delta \bar{u}_i^a), \quad \delta \theta_i \approx N_i^a \mathcal{I}(\delta \bar{\theta}_i^a), \quad \delta \varphi_i \approx N_i^a \mathcal{I}(\delta \bar{\varphi}_i^a), \end{aligned} \tag{27}$$

where \mathcal{I} denotes a complex number. The residuals at each node a are obtained by introducing the discretisations of (27) in the weak forms of (26) to give:

$$\begin{aligned} R_{u_i}^a &= - \int_{\Omega_e} \mathcal{B}_{iJ}^a \sigma_J \, d\Omega_e + \int_{\Omega_e} N^a f_i \, d\Omega_e + \int_{\Gamma_e} N^a t_i \, d\Gamma_e, \\ R_{\theta_i}^a &= - \int_{\Omega_e} \mathcal{B}_{iJ}^a \tau_J \, d\Omega_e - \int_{\Omega_e} N^a 2\sigma_i^\times \, d\Omega_e + \int_{\Gamma_e} N^a m_i \, d\Gamma_e, \\ R_{\varphi}^a &= - \int_{\Omega_e} \mathcal{B}_i^a B_i \, d\Omega_e, \end{aligned} \tag{28}$$

where the uppercase subscripts refer to Voigt’s notation of Table 1 and the matrices \mathcal{B}_{iJ} and \mathcal{B}_i at each local node a are:

$$[\mathcal{B}_{Ji}^a] = \begin{bmatrix} N_{,1}^a & 0 & 0 \\ 0 & N_{,2}^a & 0 \\ 0 & 0 & N_{,3}^a \\ N_{,2}^a & 0 & 0 \\ 0 & N_{,1}^a & 0 \\ 0 & N_{,3}^a & 0 \\ 0 & 0 & N_{,2}^a \\ 0 & 0 & N_{,1}^a \\ N_{,3}^a & 0 & 0 \end{bmatrix}, \quad \{\mathcal{B}_i^a\} = \left\{ \begin{matrix} N_{,1}^a \\ N_{,2}^a \\ N_{,3}^a \end{matrix} \right\}. \tag{29}$$

5.3 Tangent matrices

The complex-step method easily allows for computing the multi-coupled tangent matrices. These matrices are the derivatives of the residuals $R^a(u_b)$ for node a in terms of a generic nodal unknown u_b . Then, writing a Taylor series expansion about u_b in terms of an imaginary change of each dependent variable at node n , one may write:

$$\begin{aligned} R^a(u_b + i \delta_{bn} h_n) &= R^a(u_b) + \frac{\partial R^a}{\partial u_n} (i h_n) + \\ &\frac{1}{2!} \frac{\partial^2 R^a}{\partial u_n^2} (i h_n)^2 + \frac{1}{3!} \frac{\partial^3 R^a}{\partial u_n^3} (i h_n)^3 + \dots, \end{aligned} \tag{30}$$

which upon collecting terms, yields:

$$\begin{aligned} R^a(u_b + i \delta_{bn} h_n) &= \left[R^a(u_b) - \frac{1}{2!} \frac{\partial^2 R^a}{\partial u_n^2} h_n^2 \right] + \\ &i \left[\frac{\partial R^a}{\partial u_n} h_n - \frac{1}{3!} \frac{\partial^3 R^a}{\partial u_n^3} h_n^3 \right] + \dots, \end{aligned} \tag{31}$$

For cases where the higher derivatives are well behaved and using small values $h_n = 10^{-40}$, all residuals and tangent matrices are computed to full numerical accuracy from:

$$\begin{aligned} R^a &\approx \Re[R^a(u_b + i \delta_{bn} h_n)], \\ \frac{\partial R^a}{\partial u_n} &\approx \frac{1}{h_n} \Im[R^a(u_b + i \delta_{bn} h_n)]. \end{aligned} \tag{32}$$

This formulation is implemented into the research code *FEAP* [36] by using one of its dummy elements; the present numerical code without micro-rotations is tested against solutions of the total MST formulation developed in [26] obtaining perfect agreement. Notice that the multi-coupled tangent matrix is non-symmetric due to the inclusion of the MST and, consequently, the *FEAP* command *UTAN* must be used to invert the tangent matrix.

Table 2 Terfenol–D material properties at $|\mathbf{H}| = 100$ [kA/m] from [33]: C_{ij} stiffness, e_{ij}^φ piezo-magnetic coupling, μ_{ij} magnetic permeability and $l_b = l_t$ micromechanical characteristic lengths

| Property | Value | Unit |
|--|---------------------|--|
| $C_{11} / C_{33} / C_{44}$ | 36 / 46.5 / 4.2 | [GPa] |
| $C_{66} / C_{12} / C_{13}$ | 9.1 / 17.7 / 23.3 | [GPa] |
| $e_{31}^\varphi / e_{33}^\varphi / e_{15}^\varphi$ | −0.31 / 1.99 / 1.39 | [N/A·m] |
| μ_{11} / μ_{33} | 1.02 / 0.38 | [N·s ² /C ²] × 10 ^{−5} |
| l_b / l_t | 10 ^{−5} | [m] |

6 Numerical experiments

This section presents four numerical experiments to study the influence of the skew–symmetric part of the MST on the magneto–mechanical response in a magnetostrictive material under magnetic fields. For this purpose and as in [26], a magnetostrictive rod of length 6 [mm] and diameter 2 [mm] is simulated. The rod is made out of the alloy Terfenol–D, with properties listed in Table 2; the order of magnitude for l_b , l_t is taken from [3] for the crystal grains of many magnetic materials.

This alloy presents transversely isotropic planes x_1 – x_2 since the magnetisation M_3 is along the x_3 axis, see the Fig. 4; therefore, the planes containing x_3 are anisotropic.

The skew–symmetric MST plays an essential role in activating the rotations as long as two conditions are met:

- The magnetic field H_i interacts with an anisotropic plane, not with the transversely isotropic plane.
- The field is oblique to this anisotropic plane.

The idea is to prescribe an H_i that activates the skew–symmetric term σ_i^x of (20), generating couple stresses τ_{ji} and therefore micro–rotations θ_i . These rotations are closely related to the existence of the microstructure, introduced in the FE model by the l_b and l_t scale parameters in the third tensor of the Appendix 1.

For all numerical experiments, the rod geometry is discretised by a FE mesh composed of 3,840 eight–noded elements, including 6,300 nodal points with seven dofs, as shown in Fig. 4 left. The mechanical dofs u_i and θ_i are fixed at the rod bottom, the rest are free. Since the present is a displacement–based FE formulation, no tractions are prescribed due to the absence of mechanical forces or pressures.

To prescribe nonuniform magnetic fields for the first three experiments with the FE method, a discretised air domain with dimensions $3 \times 3 \times 6$ [mm] wraps the Terfenol–D rod: the additional mesh of 2,560 elements and 4,200 nodes is represented in Fig. 4 right. The vacuum permeability of air is $\mu_0 = 1.256 \times 10^{-6}$ [N/A²], and its mechanical dofs from

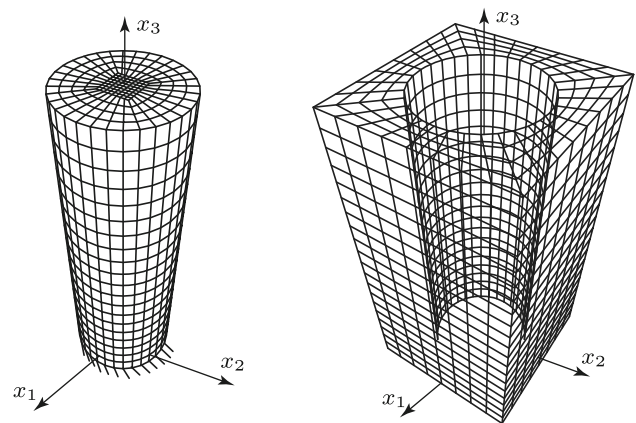


Fig. 4 Finite element mesh of the Terfenol–D rod (left) for all numerical experiments; finite element mesh of air (right) for numerical experiments 1 to 3

Table 3 For Fig. 4 left, definition of external faces by constant coordinates in [mm], and prescribed magnetic potential φ in [A] for three numerical experiments

| Face | Expr. 1 | Expr. 2 | Expr. 3 |
|--------------|---------|---------|---------|
| $x_1 = 1.5$ | 0 | − 10 | − 10 |
| $x_1 = -1.5$ | 0 | − 10 | 0 |
| $x_2 = 1.5$ | − 10 | free | free |
| $x_2 = -1.5$ | − 10 | free | free |
| $x_3 = 0$ | free | 0 | 0 |
| $x_3 = 6$ | free | 0 | 0 |

the coupled FE of Sect. 5 are deactivated so that only one FE type is used though the analyses for both materials.

In Table 3, the magnetic boundary conditions for the cases in the next subsections are listed; if no prescription is applied, the word “free” is indicated.

6.1 Magnetic field in transversely isotropic planes

The quadrupole magnetic field reported in [5] is chosen for the first three experiments. In the laboratory, the quadrupole is created by four magnets arranged so that \mathbf{H} varies with the radial distance in planes x_1 – x_2 , but the field is constant along the x_3 axis. The magnetic potential boundary conditions are sketched in Fig. 5 left and listed in Table 3, producing a field that curves from one vertical side to the contiguous one (centre figure): then, $H_1 \approx H_2$ and $H_3 = 0$. The field is almost axisymmetric, as seen in the figure of the right for \mathbf{H} (smoothed through the whole mesh by the SPSVERBa1 software). But the critical domain is the Terfenol–D rod, where the field is uniform.

The maximum generated \mathbf{H} is 22 [kA/m], a value that could be obtained by a commercial magneto cell under an electric intensity of only 5 [A].

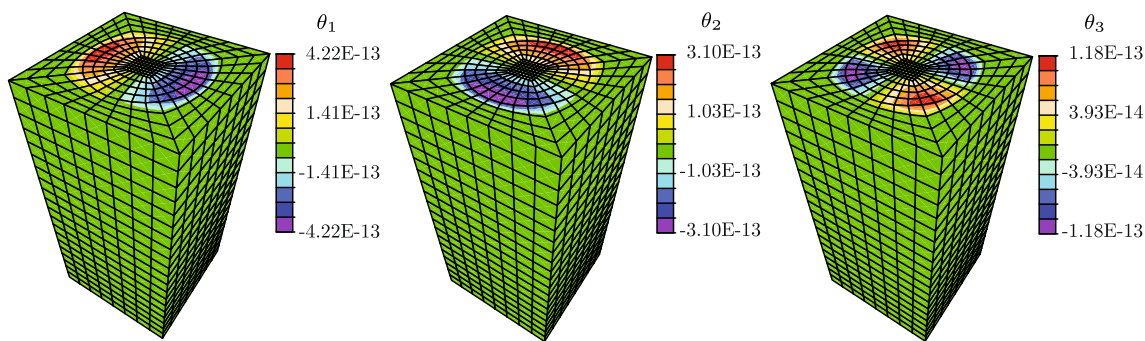


Fig. 5 Quadrupole magnetic field. Boundary conditions of magnetic scalar potential φ in [A] applied to external vertical sides (left); direction of the magnetic field lines (centre); contour plot of the resulting magnetic field module in [A/m] (right). External dimensions $3 \times 3 \times 6$ [mm]

Table 4 Calculation time (with respect to CCM–w/o) to solve the numerical experiment of Fig. 5 with three models. Number of Newton–Raphson iterations and converged residual norm for each experiment

| Model | Relative CPU | # iter. | Residual norm |
|---------|--------------|---------|------------------------|
| CCM–w/o | 1 | 1 | 1.69×10^{-16} |
| CCM–w | 1.5 | 2 | 1.82×10^{-17} |
| GCM | 6.3 | 2 | 1.82×10^{-17} |

Figure 6 shows the resulting contour plots for the three micro–rotations θ_i generated inside the rod. As observed in the figure and expected, the micro–rotations are strictly zero in the air (green level) since its mechanical rigidity is null. The order of magnitude inside the Terfenol–D is 10^{-13} [rad], not zero but almost numerical noise. This result is logical since under the quadrupole the magnetic field is contained in the transversely isotropic planes x_1 – x_2 , and no rotations are activated as it will be demonstrated in (36).

The main shortcoming of the present MM formulation is the necessary CPU time: Table 4 shows the calculation times of three models for the current numerical experiment. The first row is for CCM without Maxwell stress tensor (CCM–w/o), the second for CCM with total Maxwell stress (CCM–w), and the third for the present GCM.

All simulations are executed in a dual–core Intel Core i5–2500T running at 2.3 [GHz]. For the first two models, the FE element developed in [26] was used with the mesh of Fig. 4.

As observed, the CPU time is substantially higher for MM, mainly because the three micro–rotations are extra nodal unknowns. The dofs are the same for the CCM–w/o and CCM–w models; however, the CPU time differs due to the non–linearity of the MST, which requires one more Newton–Raphson iteration. In this context, SPSVERBa1 calculates for all models the value:

$$val = \frac{\|\mathcal{R}^{k+1}\|}{\|\mathcal{R}^0\|} \leq tol, \tag{33}$$

The residuals’ superscripts $k + 1$ and 0 refer to the current and the first iterations, respectively. The solution is reached when *val* is lower than the computer–dependent tolerance $tol = 10^{-16}$.

6.2 Symmetric magnetic field in anisotropic planes

With the previous mesh, the micro–rotations are now studied with the boundary conditions of Fig. 7 left and of Table 3. Now \mathbf{H} varies in the vertical planes but not in the horizontal ones. In this way, the magnetic field curves from $\varphi = 0$ [A] to all planes but primarily to the vertical ones crossing the anisotropic planes as in the centre figure.

In Fig. 8, the resulting rotations are plotted. The micro–rotation θ_3 is again only numerical noise (almost zero) since the only magnetic field to produce this component would be in the isotropic plane x_1 – x_2 (of the Sect. 6.1 type), but as mentioned and demonstrated in Sect. 6.4, these fields do not create micro–rotations. The other two components are six or seven orders of magnitude higher than those of Sect. 6.1, thanks to the prevalence of the H_3 component; H_1 is also high but only at the edges of x_1 constant. The value of θ_2 is almost three times larger than that of θ_1 due to the magnetic field concentration on some of the edges.

In any case, the micro–rotations are still much smaller than expected for an \mathbf{H} partially applied in an anisotropic plane. There are two reasons for these low values: i) the perpendicularity of \mathbf{H} to the planes x_1 – x_2 in some zones of the rod, and ii) the symmetry of this field that partially cancels θ_1 and θ_2 since the field concentrations at edges of the plane $x_1 = 1.5$ equilibrates the effect of the other concentrations at $x_1 = -1.5$, see the Fig. 7 right.

6.3 Nonsymmetric magnetic field in anisotropic planes

Again, with the quadrupole set, the micro–rotations are partially activated in this experiment. In Fig. 9 left, the boundary conditions are changed so that \mathbf{H} varies in the vertical planes

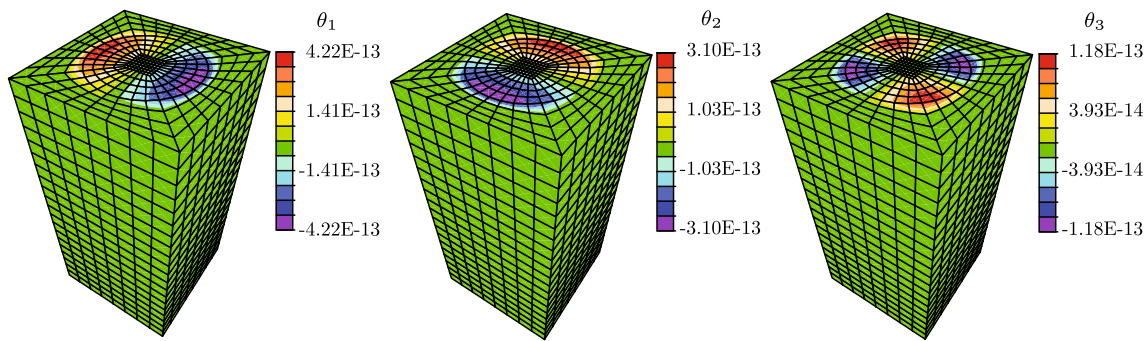


Fig. 6 Terfenol–D rod wrapped by air under the nonuniform magnetic field of Fig. 5. Contour plots of micro–rotations in radians generated by the skew–symmetric part of the Maxwell stress tensor

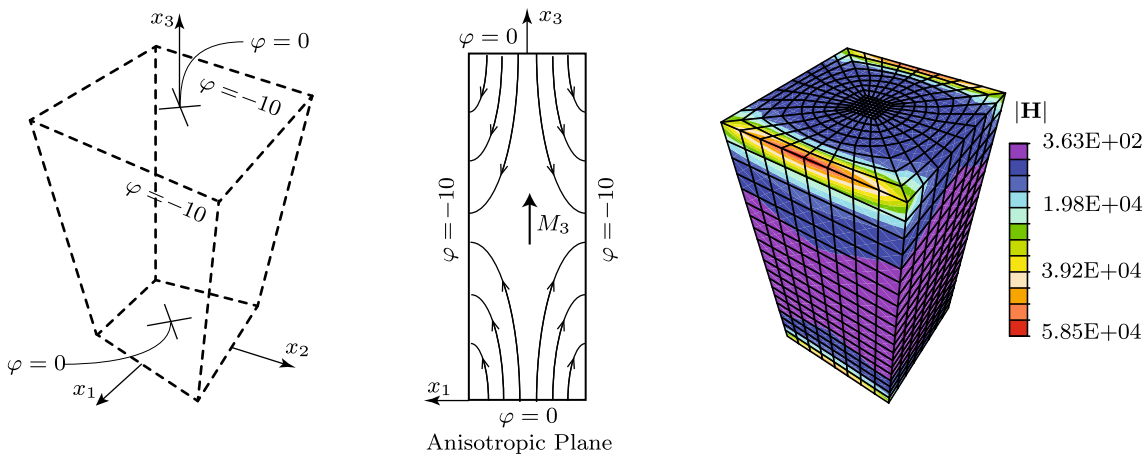


Fig. 7 Modified quadrupole magnetic field. Boundary conditions of magnetic scalar potential φ in [A] applied to external sides (left); direction of the magnetic field lines (centre); contour plot of the resulting magnetic field module in [A/m] (right). External dimensions $3 \times 3 \times 6$ [mm]

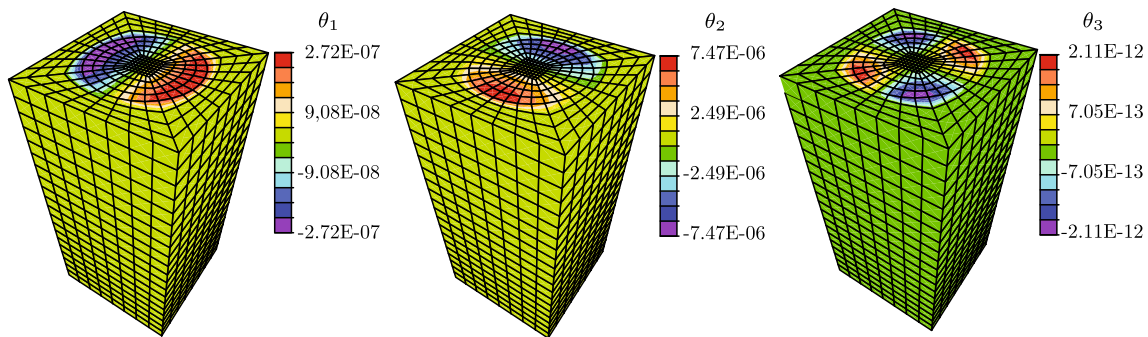


Fig. 8 Terfenol–D rod wrapped by air under a nonuniform magnetic field of Fig. 7. Contour plots of micro–rotations in radians generated by the skew–symmetric part of the Maxwell stress tensor. In the central figure, only the solid is represented

but now without vertical symmetry. With the prescribed boundary conditions of Table 3, the magnetic field curves from the $\varphi = -10$ [A] face towards all others in the whole domain.

In Fig. 10, the three rotations are represented: θ_1 is still not activated, but θ_2 is already a measurable 0.01° , and again θ_3 is practically zero. The reason for $\theta_2 > \theta_1$ is that most of the magnetic field curves in the x_2 -constant vertical plane to the

external face. In addition, the micro–rotation concentrates close to the face under $\varphi = -10$ [A] for the same reason, and any other rotation does not cancel it.

In the central figure of the highest component θ_2 , only the Terfenol–D part of the mesh has been represented to appreciate that the micro–rotation of the solid is uniform in horizontal planes and non–linear to fulfil the zero boundary condition at the rod base plus the free movement at the top.

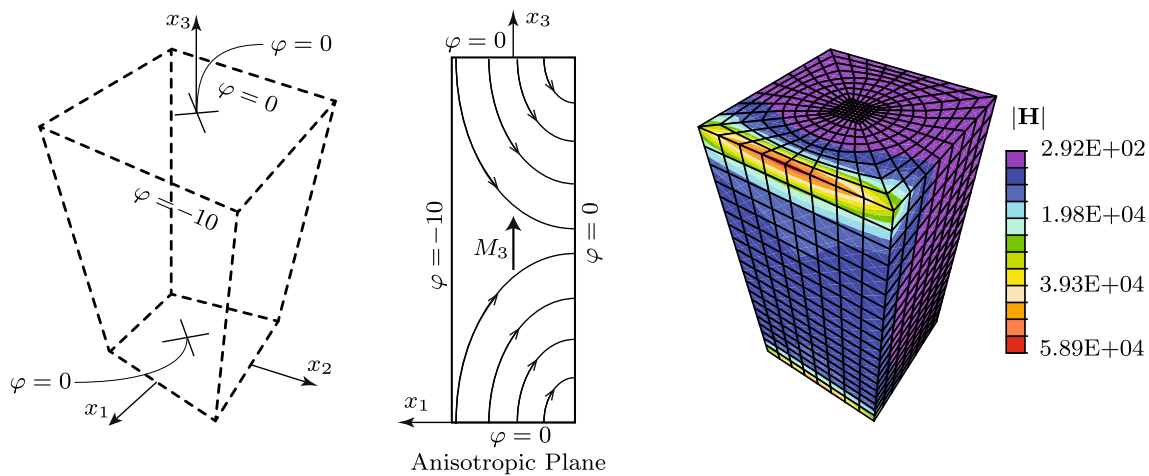


Fig. 9 Modified quadrupole magnetic field. Boundary conditions of magnetic scalar potential ϕ in [A] applied to external sides (left); direction of the magnetic field lines (centre); contour plot of the resulting magnetic field module in [A/m] (right). External dimensions $3 \times 3 \times 6$ [mm]

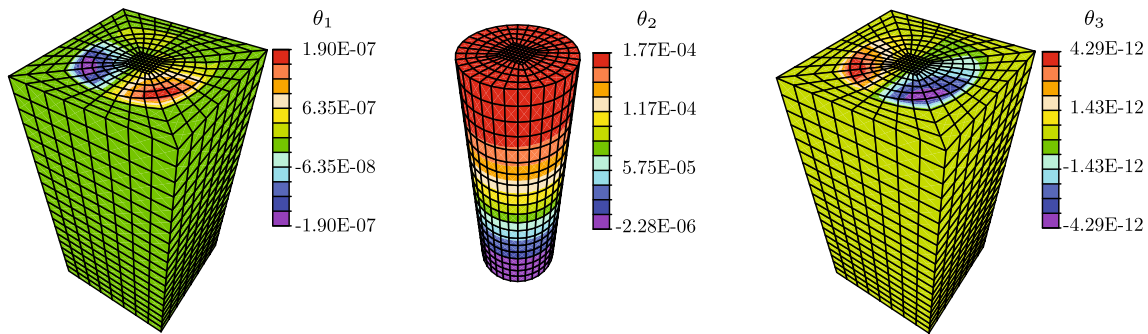


Fig. 10 Terfenol-D rod wrapped by air under a nonuniform magnetic field of Fig. 9. Contour plots of micro-rotations in radians generated by the skew-symmetric part of the Maxwell stress tensor. In the central figure, only the solid is represented

Although appreciable, these micro-rotations are still small since the magnetic field is primarily parallel (not oblique) to the vertical anisotropic planes in the central part of the rod.

Figure 11 presents two distributions: the left one relates the intensity of the magnetic potential up to a value of -50 [A] (achievable with commercial magnets) against the maximum θ_2 of Fig. 10 centre in absolute value. The trend is approximately quadratic, producing a substantial 25 increase in rotations for only five in magnetic potential.

As commented before, the micro-rotations depend on the micro-scale parameters $l_b = l_t$. For this reason and to study their influence on θ_2 , the right Fig. 11 plots the order of magnitude of the maximum micro-rotation versus the order of magnitude of l_b . These rotations range from a non-physical 10^5 for very low l_b to an almost zero 10^{-10} [rad] for very high l_b ; the real values given in [3] range from 10^{-4} to 10^{-6} .

To understand the linearity of the result, consider the equations that govern the macro-mechanical bending of a beam:

$$\left. \begin{aligned} \frac{\partial M_b}{\partial x} &= m_b \\ M_b &= EI \frac{\partial \phi}{\partial x} \end{aligned} \right\} \Rightarrow \phi = \frac{m_b}{2EI} x^2, \quad (34)$$

with M_b , m_b , E , I , and ϕ denoting bending moment, moment source, Young modulus, second moment of area, and cross-section rotation in any plane, respectively. The integration of ϕ does not conserve constants due to the “cantilever”-type boundary conditions of Fig. 4.

For the current MM analogy, m is closely related to the skew-symmetric part of the MST and I to the bending scale length l_b , which can be interpreted as the inertia of the micro-continuum. Consequently, the maximum of the three rotations from Fig. 7 (right) inversely depends on l_b as in (34), that is, the lower its value, the higher the micro-rotations and the relationship is linear.

6.4 Uniform oblique magnetic field in anisotropic planes

The objective of the last numerical experiment is to analyse the influence of a completely oblique magnetic field on the generation of substantial micro-rotations. The importance of this study is that, for real materials, the initial magnetisation direction M_3 of the grains can rotate a different amount under the presence of a variable \mathbf{H} , provoking the domain

Fig. 11 For experiment of Fig. 9: left: absolute value of maximum micro-rotation in plane x_1-x_3 versus prescribed magnetic potential; right: exponent of 10 for micro-rotation versus same exponent for microstructure scale parameter

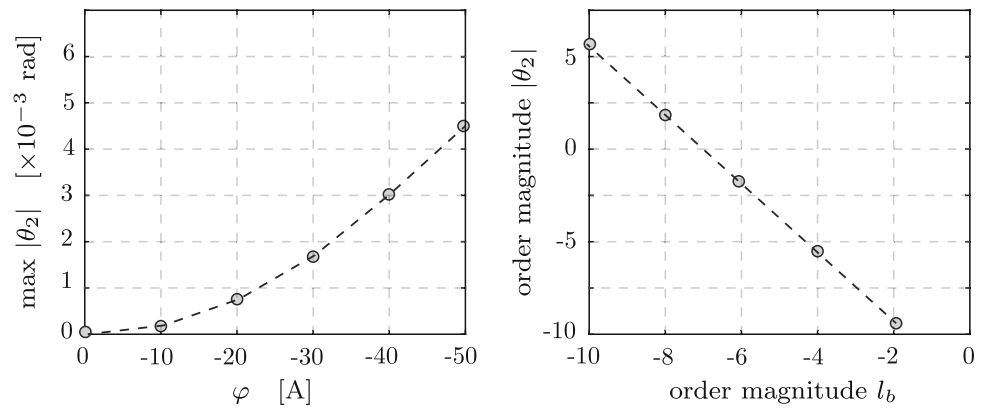
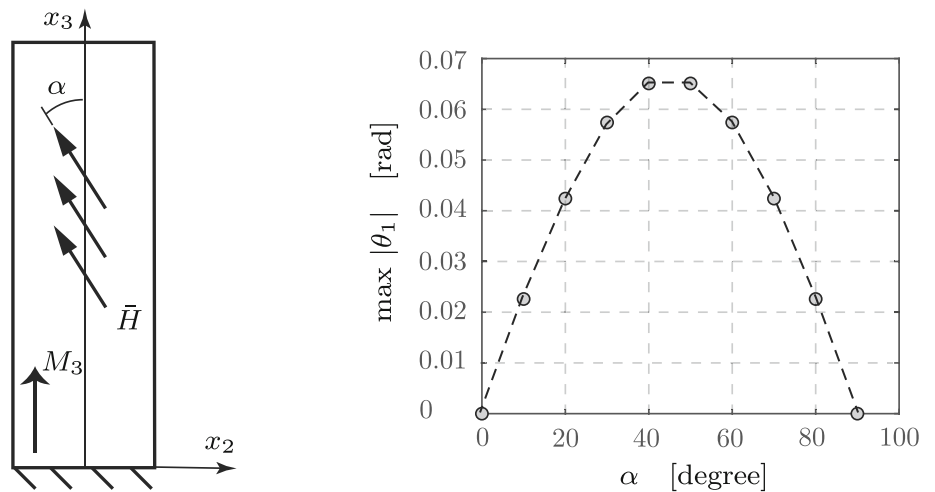


Fig. 12 Left: Applied magnetic field \vec{H} function of the angle α . The M_3 vector denotes the magnetisation direction of the Terfenol-D rod. Right: Maximum micro-rotation in absolute value in plane x_2-x_3 versus α



switch phenomena and changing the macroscopic response of magnetostrictives.

As observed in the left Fig. 12, the numerical experiment considers the Terfenol-D rod magnetised along x_3 under the action of an oblique and constant magnetic field function of the variable angle α . A vertical $H_3 = 22$ [kA/m] is first considered; to study the effect of different directions of the magnetic field in the plane x_2-x_3 , a rotation with a variable angle α is calculated:

$$\begin{Bmatrix} \vec{H}_1 \\ \vec{H}_2 \\ \vec{H}_3 \end{Bmatrix} = \begin{bmatrix} 1 & 0 & 0 \\ 0 & \cos \alpha & -\sin \alpha \\ 0 & \sin \alpha & \cos \alpha \end{bmatrix} \begin{Bmatrix} 0 \\ 0 \\ H_3 \end{Bmatrix}, \tag{35}$$

Although the present FE is not mixed and, therefore, first derivatives cannot directly be prescribed, thanks to the fully nonlinear formulation, the calculated $\vec{H}_1, \vec{H}_2, \vec{H}_3$ are introduced in the SPSVERBa1 input as Neumann boundary conditions. Then, they can be automatically assigned to the nodal values of the magnetic field during the first iteration.

Figure 12 right plots the calculated maximum micro-rotation inside the rod in absolute value versus α . As observed, the micro-rotations are null for both $\alpha = 0^\circ$ and $\alpha = 90^\circ$ since the applied magnetic field is parallel (almost

as in Sect. 6.2) and perpendicular (as in Sect. 6.1) to M_3 . Increasing α from zero, the micro-rotations increase to a maximum of 0.0665 [rad] for $\alpha = 45^\circ$.

The explanation of this distribution can be found in the second (18), which can be expanded to:

$$\begin{Bmatrix} \tau_{11,1} + \tau_{21,2} + \tau_{31,3} \\ \tau_{12,1} + \tau_{22,2} + \tau_{32,3} \\ \tau_{13,1} + \tau_{23,2} + \tau_{33,3} \end{Bmatrix} + \begin{Bmatrix} B_2 \vec{H}_3 - B_3 \vec{H}_2 \\ B_3 \vec{H}_1 - B_1 \vec{H}_3 \\ B_1 \vec{H}_2 - B_2 \vec{H}_1 \end{Bmatrix} = \begin{Bmatrix} 0 \\ 0 \\ 0 \end{Bmatrix}, \tag{36}$$

where the diagonal entries τ_{ii} can be regarded as MM torsional moments and the off-diagonal τ_{ij} as MM bending moments. Consider first that B_i is approximately proportional to H_i ($u_{j,k}$ is very small); then the second and third entries of the second vector at the left-hand side of (36) are zero (in this experiment $\forall \alpha \rightarrow \vec{H}_1 = 0$ and therefore $B_1 \approx 0$). Since from Table 2 $\mu_{22} = \mu_{11} = 2.68\mu_{33}$, the non-zero components \vec{H}_3 and \vec{H}_2 of Fig. 12 contribute to the first entry as:

$$B_2 \vec{H}_3 - B_3 \vec{H}_2 \approx -4230 \sin \alpha \cos \alpha \tag{37}$$

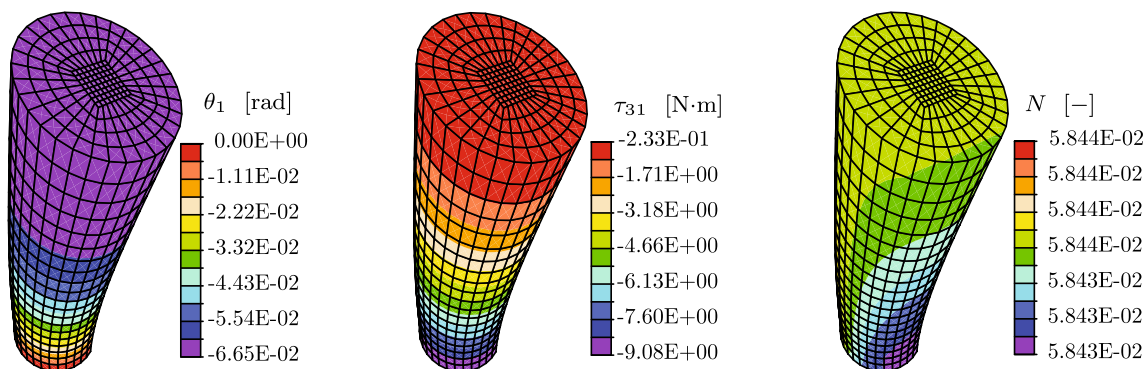


Fig. 13 Contour plots of micro-rotation θ_1 (left), couple stress τ_{31} (middle) and contribution of skew-symmetric MST from (38) (right) all for angle $\alpha = 45^\circ$ of Fig. 12 left. Deformed meshes magnified by a factor of 50,000

The right-hand side previous equation is maximum at $\alpha = 45^\circ$ and zero at $\alpha = 0^\circ$ or 90° (vertical or horizontal \vec{H} respectively), values that explain the maximum and minimums of Fig. 12 right. These two values also explain the nullity of the micro-rotations of Fig. 6 and, in part, the low values of Fig. 9, since for these angles, the second vector of the (36) right-hand side is nil. In these two experiments, the three equations give the trivial solution $\tau_{ji} = 0$, and without source, all micro-rotations are zero.

The discussion of (36) is qualitative but not quantitative: the difficulty lies in finding the distribution of the rotations inside the Terfenol-D rod, for which the present numerical method is necessary. Figure 13 shows FE contour plots (deformed mesh with zoom $\times 50,000$) generated with the boundary conditions of Fig. 12. In the left figure, a non-linear distribution is observed due to the clamped fixation of the rod at the bottom end. The same non-linearity is observed for the τ_{31} component of the couple stress in the central figure, with a non-negligible reaction of 9.1 [N·m] at the fixed end; the deformed mesh shows a global bending of the rod, a shape that cannot be produced with, for instance, the CCM model.

To quantify the influence of the MST skew-symmetric part, the Fig. 13 right shows a ratio between the Frobenius norm of $\sigma_{[ji]}^{EM}$ and that of σ_{ji}^{EM} :

$$N = \frac{\sqrt{\text{trace}(\sigma_{[ij]}^{EM} \sigma_{[ji]}^{EM})}}{\sqrt{\text{trace}(\sigma_{ij}^{EM} \sigma_{ji}^{EM})}} \tag{38}$$

The figure shows that the ratio is approximately constant since the applied magnetic field is also constant in the bar. The MST skew-symmetric part is significant given that it generates about 6% of the total.

One interesting outcome of the present study is that the mentioned “domain switching” phenomena could be explained with the micro-rotations and the influence of the

magnetic dipoles’ rotation on the magnetic material properties. These investigations will be studied in future work.

7 Concluding remarks

The present article has presented a theoretical and numerical formulation based on the finite element method to investigate the influence of the non-symmetry of the Maxwell stress tensor. This tensor contains a skew-symmetric contribution necessary for the study of rotations in non-isotropic materials; physically, these local rotations arise from the conservation of angular momentum.

In the framework of classical continuum mechanics, the total stress tensor formulation allows for calculating displacements of the center of mass at each material point but does not calculate rotations. On the contrary, extended formulations such as the current generalised continuum mechanics take into account the skew-symmetric part of the Maxwell tensor, which generates local rotations and couple stresses.

Numerically, a three-dimensional finite element formulation with seven degrees of freedom (three displacements, three micro-rotations, and the magnetic scalar potential) using a complex-step approach for the tangent matrices has been formulated and implemented in the research finite element code *FEAP*.

Four numerical experiments have been studied to extract the following consequences:

- The skew-symmetric part of the Maxwell stress tensor generates both micro-rotations and couple stresses that depend on i) scale parameters (microsize-dependency) closely related with the internal structure of the magnetic materials and ii) orientation of the prescribed magnetic field.

- In the classical continuum mechanics framework, the scale parameters of i) are null and, therefore, there are no micro-rotations.
- The dependency of ii) could explain the highly non-linear domain switching mechanisms in magnetostrictive/electrostrictive materials since the rotations of the internal grains change the magnetisation/polarisation of materials.
- For a magnetic field of 22 [kA/m] and for Terfenol-D material, the order of magnitude of these micro-rotations is up to 0.066 radians and its corresponding couple stress -9 [N·m].

In summary, the skew-symmetric part of the Maxwell tensor is a relevant 6% of the total. Therefore this part should be considered in modern and sophisticated electro-magneto-mechanical devices.

Funding Funding for open access publishing: Universidad de Granada/CBUA.

Open Access This article is licensed under a Creative Commons Attribution 4.0 International License, which permits use, sharing, adaptation, distribution and reproduction in any medium or format, as long as you give appropriate credit to the original author(s) and the source, provide a link to the Creative Commons licence, and indicate if changes were made. The images or other third party material in this article are included in the article's Creative Commons licence, unless indicated otherwise in a credit line to the material. If material is not included in the article's Creative Commons licence and your intended use is not permitted by statutory regulation or exceeds the permitted use, you will need to obtain permission directly from the copyright holder. To view a copy of this licence, visit <http://creativecommons.org/licenses/by/4.0/>.

A constitutive matrices

This appendix reports the matrix forms of the constitutive equations used in the present work.

$$[C_{ijkl}] = \begin{bmatrix} C_{11} & C_{12} & C_{13} & 0 & 0 & 0 & 0 & 0 & 0 \\ C_{12} & C_{11} & C_{13} & 0 & 0 & 0 & 0 & 0 & 0 \\ C_{13} & C_{13} & C_{33} & 0 & 0 & 0 & 0 & 0 & 0 \\ 0 & 0 & 0 & C_{66} & C_{66} & 0 & 0 & 0 & 0 \\ 0 & 0 & 0 & C_{66} & C_{66} & 0 & 0 & 0 & 0 \\ 0 & 0 & 0 & 0 & 0 & C_{44} & C_{44} & 0 & 0 \\ 0 & 0 & 0 & 0 & 0 & C_{44} & C_{44} & 0 & 0 \\ 0 & 0 & 0 & 0 & 0 & 0 & 0 & C_{44} & C_{44} \\ 0 & 0 & 0 & 0 & 0 & 0 & 0 & C_{44} & C_{44} \end{bmatrix},$$

$$[e_{ijk}^{\varphi}] = \begin{bmatrix} 0 & 0 & 0 & 0 & 0 & 0 & 0 & 0 & 0 \\ 0 & 0 & 0 & 0 & 0 & e_{15}^{\varphi} & e_{15}^{\varphi} & 0 & 0 \\ e_{31}^{\varphi} & e_{31}^{\varphi} & e_{33}^{\varphi} & 0 & 0 & 0 & 0 & e_{15}^{\varphi} & e_{15}^{\varphi} \end{bmatrix},$$

$$[\mu_{ij}] = \begin{bmatrix} \mu_{11} & 0 & 0 \\ 0 & \mu_{11} & 0 \\ 0 & 0 & \mu_{33} \end{bmatrix},$$

$$[C_{ijkl}^*] = \begin{bmatrix} C_{11}^* & 0 & 0 & 0 & 0 & 0 & 0 & 0 & 0 \\ 0 & C_{11}^* & 0 & 0 & 0 & 0 & 0 & 0 & 0 \\ 0 & 0 & C_{33}^* & 0 & 0 & 0 & 0 & 0 & 0 \\ 0 & 0 & 0 & C_{66}^* & 0 & 0 & 0 & 0 & 0 \\ 0 & 0 & 0 & 0 & C_{66}^* & 0 & 0 & 0 & 0 \\ 0 & 0 & 0 & 0 & 0 & C_{44}^* & 0 & 0 & 0 \\ 0 & 0 & 0 & 0 & 0 & 0 & C_{44}^* & 0 & 0 \\ 0 & 0 & 0 & 0 & 0 & 0 & 0 & C_{44}^* & 0 \\ 0 & 0 & 0 & 0 & 0 & 0 & 0 & 0 & C_{44}^* \end{bmatrix},$$

with $C_{11}^* = C_{44}l_t^2$, $C_{33}^* = C_{66}l_t^2$, $C_{66}^* = C_{66}l_b^2$ and $C_{44}^* = C_{44}l_b^2$.

References

1. Bustamante R, Dorfmann A, Ogden RW (2009) Nonlinear electroelastostatics: a variational framework. *Z Angew Math Phys* 60:154–177
2. Dorfmann A, Ogden RW (2005) Nonlinear electroelasticity. *Acta Mech* 174:167–183
3. Dunlop DJ, Özdemir Ö (2001) Rock magnetism: fundamentals and frontiers. Cambridge University Press, Cambridge
4. Eringen AC, Maugin GA (1990) Electrodynamics of Continua I. Springer-Verlag, New York Inc
5. Ghaith A, Oumbarek D, Kitégi C, Valléu M, Martes F, Couprie ME (2019) Permanent magnet-based quadrupoles for plasma acceleration sources. *Instruments* 3:27
6. Henrotte DF, Hameyer K (2007) On the local force computation of deformable bodies in magnetic field. *IEEE Trans Magn* 43(4):1445–1448
7. Ivanova EA, Kolpakov YE (2013) The use of moment theory to describe the piezoelectric effect in polar and non-polar materials 163–178
8. Jiménez JL, Campos I, López-Mari MA (1982) The Minkowski and Abraham tensors, and the non-uniqueness of non-closed systems. *Int J Eng Sci* 20(11):1193–1213
9. Jiménez JL, Campos I (2013) Maxwell's equations in material media, momentum balance equations and force densities associated with them. *Eur Phys J Plus* 128(46):1–6
10. Juretschke HJ (1977) Simple derivation of the Maxwell stress tensor and electrostrictive effects in crystals. *Am J Phys* 45(3):277–280
11. Kannan KS, Dasgupta A (1997) A nonlinear galerkin finite-element theory for modeling magnetostrictive smart structures. *Smart Mater Struct* 6:341–350
12. Kim S, Ryu J, Cho M (2011) Numerically generated tangent stiffness matrices using the complex variable derivative method for nonlinear structural analysis. *Comput Methods Appl Mech Eng* 200:403–413
13. Kloos G (1998) Magnetostatic Maxwell stresses and magnetostriction. *Electr Eng* 81:77–80
14. Kuang ZB (2008) Some variational principles in elastic dielectric and elastic magnetic materials. *Eur J Mech A Solids* 27(3):504–514
15. Landau LD, Lifshitz, EM (1984) In *Electrodynamics of Continuous Media (Second Edition)*, volume 8 of *Course of Theoretical Physics*. Pergamon, second edition

16. Lyness JN, Moler CB (1967) Numerical differentiation of analytic functions. *SIAM J Numer Anal* 4:202–210
17. Maugin GA, Metrikine AV (2010) *Mechanics generalized continua: One hundred years after the Cosserats*. Springer-Verlag, New York Inc
18. McGregor M, Wheel MA (2014) On the coupling number and characteristic length of micropolar media of differing topology. *Proc R Soc A* 470:20140150
19. McMeeking RM, Landis CM (2005) Electrostatic forces and stored energy for deformable dielectric materials. *J Appl Mech* 72(4):581–590
20. Melcher JR (1981) *Continuum electromechanics*. MIT Press, Cambridge, Mass
21. Michelitsch TM, Maugin GA, Derogar MRS, Nowakowski AF, Nicolleau FCGA (2012) An approach to generalized one-dimensional self-similar elasticity. *Int J Eng Sci* 61:103–111
22. Miehe C, Kiefer B, Rosato D (2011) An incremental variational formulation of dissipative magnetostriction at the macroscopic continuum level. *Int J Solids Struct* 48(13):1846–1866
23. Moreno-Navarro P, Ibrahimbegovic A, Pérez-Aparicio JL (2017) Plasticity coupled with thermo-electric fields: Thermodynamics framework and finite element method computations. *Comput Methods Appl Mech Eng* 315:50–72
24. Nelson DF Asymmetric total stress tensor. *Phys Rev B*, 13(4):0-1976
25. Nishiguchi I, Kameari A, Haseyama K (1999) On the local force computation of deformable bodies in magnetic field. *IEEE Trans Magn* 35(3):1650–1653
26. Palma R, Pérez-Aparicio JL, Taylor RL (2020) Non-linear and hysteretical finite element formulation applied to magnetostrictive materials. *Comput Mech* 65:1433–1445
27. Pao Y, Hutter K (1975) Electrodynamics for moving elastic solids and viscous fluids. *Proc IEEE* 63(7):1011–1021
28. Perez-Aparicio JL, Palma R, Taylor RL (2016) Multiphysics and thermodynamic formulations for equilibrium and non-equilibrium interactions: non-linear finite elements applied to multi-coupled active materials. *Archives of Computational Methods in Engineering*, pp 535–583
29. Perez-Aparicio JL, Sosa H, Palma R (2007) Numerical investigations of field-defect interactions in piezoelectric ceramics. *Int J Solids Struct* 44(14–15):4892–4908
30. Poya R, Gil AJ, Ortigosa R, Palma R (2011) On a family of numerical models for couple stress based flexoelectricity for continua and beams. *J Mech Phys Solids* 125:613–652
31. Rinaldi C, Brener H (2002) Body versus surface forces in continuum mechanics: Is the maxwell stress tensor a physically objective cauchy stress? *Phys Rev E* 65:036615
32. Rus G, Palma R, Perez-Aparicio JL (2009) Optimal measurement setup for damage detection in piezoelectric plates. *Int J Eng Sci* 47(4):554–572
33. Sherman CH, Butler JL (2007) *Transducers and Arrays for Underwater Sound*. Springer, New York
34. Spalek D (2013) Two theorems about lorentz method for asymmetrical anisotropic regions. *Bulletin of the Polish Academy Sciences* 61(2):399–404
35. Tanaka M, Fujikawa M, Balzani D, Schröder J (2014) Robust numerical calculation of tangent moduli at finite strains based on complex-step derivative approximation and its application to localization analysis. *Comput Methods Appl Mech Eng* 269:454–470
36. Taylor RL, Govindjee S (2020) FEAP A Finite Element Analysis Program, Programmer Manual. <http://projects.ce.berkeley.edu/feap>
37. Vandeveld L, Melkebeek JAA (2001) Magnetic forces and magnetostriction in ferromagnetic material. *COMPEL Int J Comput Math Electric Electron Eng* 20(1):32–51
38. Vu DK, Steinmann P, Possart G (2007) Numerical modelling of non-linear electroelasticity. *Int J Numer Meth Eng* 70:685–704
39. Zhen-Bang K (2007) Some problems in electrostrictive and magnetostrictive materials. *Acta Mech Solida Sin* 20(3):219–227

Publisher's Note Springer Nature remains neutral with regard to jurisdictional claims in published maps and institutional affiliations.